

INTEGRAL FIELD SPECTROSCOPY OF THE EXTENDED EMISSION-LINE REGION OF 3C 249.1¹

HAI FU AND ALAN STOCKTON

Institute for Astronomy, University of Hawaii, 2680 Woodlawn Drive, Honolulu, HI 96822

Accepted by ApJ

ABSTRACT

We present Gemini Multiobject Spectrograph integral field spectroscopy of the extended emission-line region associated with quasar 3C 249.1. The kinematics of the ionized gas measured from the [O III] λ 5007 line is rather complex and cannot be explained globally by a simple dynamical model, but some clouds can be modeled individually as having locally linear velocity gradients. The temperatures of the ionized gas appear uniform (varying from ~ 12000 to 15000 K), while the densities vary from a few tens to a few hundreds cm^{-3} . The emission mechanism of all of the emission clouds, as indicated by the line-ratio diagnostics, is consistent both with “shock + precursor” and pure photoionization models. The total mass of the ionized gas is on the order of $10^9 M_{\odot}$. We estimate the bulk kinetic energy and momentum of the extended emission-line region of 2.5×10^{57} ergs and 10^{50} dyne s, and a dynamical timescale of ~ 10 Myr. By comparing the injection rates of kinetic energy and momentum of different galactic wind models with the observation, we argue that the emission-line clouds are most likely a direct result from the feedback of the quasar. We also discuss the nature of the extended X-ray emission surrounding the quasar.

Subject headings: galaxies:interactions — quasars: individual(3C 249.1)

1. INTRODUCTION

About a third of low-redshift ($z \leq 0.45$) steep-spectrum radio-loud quasars are surrounded by luminous emission-line regions that often extend to several tens of kpc from the nucleus (Stockton & MacKenty 1987). The morphologies of these extended emission-line regions (EELRs) are often complex and clearly display a non-equilibrium situation showing strings of knots and filaments straddling tens of kpc, and they are in general uncorrelated with either the distribution of stars in the host galaxy or the structure of the extended radio source, if present.

The origin of the gas comprising these EELRs remains uncertain. The apparent correlation between the occurrence of EELRs and evidence for strong interaction inspired the idea that the gas is tidally disrupted material from a disk (Stockton & MacKenty 1987). But this is unlikely because (1) there is generally no correlation between stellar tidal features and the distribution of the gas, and (2) some confinement mechanism is required for the gas to retain the densities implied by the emission-line spectra for more than a very brief time ($\sim 10^4$ – 10^6 years; Fabian et al. 1987; Stockton et al. 2002). It has also been suggested that the gas comes from a cooling flow in a hot halo surrounding the quasar (Fabian et al. 1987). This scenario has been ruled out by deep *Chandra* X-ray observations of four quasars showing strong EELRs, since the hot (10^8 K) halo gas from which the warm emission-line gas is suggested to condense is not detected, indicating strong cooling is not taking place (Stockton et al. 2006). And, in any case, the standard cooling-flow paradigm seems to have been ruled out by recent high-resolution X-ray spectroscopy (Peterson et al. 2003).

If the gas cannot come from the intergalactic medium

(IGM) through a cooling flow, then it must originate from the interstellar medium (ISM) of the quasar host galaxy. Despite the non-detection of hot gaseous halos by the *Chandra* observations, highly structured X-ray emission regions are seen around two of the four quasars surveyed. One of the plausible explanations for the X-ray emission is that it is thermal bremsstrahlung from high-speed shocks. On the other hand, detailed photoionization modeling indicates that a low-density phase ($\sim 2 \text{ cm}^{-3}$) and a high-density phase ($\sim 500 \text{ cm}^{-3}$) are needed to explain the optical spectrum of one of the EELR clouds around 4C 37.43 (E1; Stockton et al. 2002). The two phases cannot be in pressure equilibrium because their temperatures are almost the same. A reasonable possibility is that the high densities in the gas are continuously regenerated by shocks propagating through the surrounding medium.

The high-speed shocks could be driven by a galactic wind, which itself results from the feedback from the quasar (Di Matteo et al. 2005) or a vigorous starburst in the host galaxy (see Veilleux et al. 2005 for a review). This evidence of ongoing galactic winds combined with the morphological properties of EELRs thus suggest a scenario where the EELRs are a direct result of a superwind—the gas is originally the ISM in the host galaxy and has been blown out and shocked by a galactic wind; the gas is then photoionized by the UV continuum from the quasar and/or ionized by the shocks.

3C 249.1 ($z = 0.31$) is a powerful quasar, also known as PG 1100+772. Around the quasar, distinct X-ray emission regions (Stockton et al. 2006) and one of the most luminous optical EELRs at $z < 0.5$ (Stockton & MacKenty 1987) are seen extending to radial distances of tens of kpc, making it an ideal candidate for an in-depth study. In this paper, we take advantage of the simultaneous spatial and spectral coverage of integral field spectroscopy (IFS) to further explore the origin of the EELR and the extended X-ray emission around 3C 249.1. Throughout we assume a flat cosmological model with $H_0 = 70 \text{ km s}^{-1}$, $\Omega_m = 0.3$, and $\Omega_{\Lambda} = 0.7$.

2. OBSERVATIONS AND DATA REDUCTION

¹ Based on observations obtained at the Gemini Observatory, which is operated by the Association of Universities for Research in Astronomy, Inc., under a cooperative agreement with the NSF on behalf of the Gemini partnership: the National Science Foundation (United States), the Particle Physics and Astronomy Research Council (United Kingdom), the National Research Council (Canada), CONICYT (Chile), the Australian Research Council (Australia), CNPq (Brazil) and CONICET (Argentina).

3C 249.1 was observed with the Integral Field Unit (IFU) of the Gemini Multiobject Spectrograph (GMOS) on the Gemini North telescope. The queue observations were executed in the early half nights of April 7 and 8, 2005 (UT). Three exposures of 2825 s were obtained with B600/G5303 grating at a central wavelength of 6537 Å. Between exposures the telescope was offset by about $0''.4$ to improve the spatial sampling. The half-field (one slit) mode was used to cover the emission lines from [Ne V] $\lambda 3426$ to [O III] $\lambda 5007$. With this setting, we had a field-of-view (FOV) of $3''.5 \times 5''$, a wavelength range of 4400 to 7200 Å, a dispersion of $0.46 \text{ \AA pixel}^{-1}$ and an instrumental full width at half-maximum (FWHM) of 3.5 pixels (1.6 \AA). The seeing varied from $0''.8$ to $1''.0$.

The data were reduced using the Gemini IRAF data reduction package (Version 1.8). The data reduction pipeline (GFREDUCE) consists of the following standard steps: bias subtraction, cosmic rays rejection, spectral extraction, flat-fielding, wavelength calibration, sky subtraction and flux calibration. Spectra from different exposures were assembled and interpolated to construct individual datacubes (x, y, λ) with a pixel size of $0''.05$ (GFCUBE). Differential atmosphere refraction was then corrected by shifting the image slices at each wavelength to keep the location of the quasar constant. The datacubes were then binned to $0''.2$ pixels, which is the original spatial sampling of the IFU fiber-lenslet system.

Since our study focuses on the emission line gas, it is desirable to remove the light of the quasar from the datacubes. For 3C 249.1 the quasar component can be cleanly removed from the datacubes by assuming that all of the continuum in the spectra is scattered light from the quasar, because (1) previous studies have shown that the host galaxy of 3C 249.1 is very faint in optical compared with the quasar itself, and (2) extended emission line clouds usually show essentially pure emission-line spectra (*e.g.*, Stockton et al. 2002). The detailed procedure was as follows: The model quasar spectrum was derived by cubic-spline smoothing the average spectrum extracted from an aperture centered on the quasar. Then the ratio of the spectrum from each pixel to this template quasar spectrum was fit with a smooth curve comprising a small number of cubic spline pieces, and the continuum was removed by subtracting the quasar template normalized by this curve. For each spectrum, pixels near strong emission lines were excluded from the sample of the continuum fitting, and the locations of these spectral regions were determined by measuring the wavelength of the [O III] $\lambda 5007$ line from each residual spectrum. These steps were repeated a few times to achieve best residual datacubes. Finally, the residual datacubes were smoothed to a common spatial resolution, and merged to a final datacube. We generated exposure maps for each wavelength to account for the exposure time variation caused by the dithering and the differential atmosphere refraction.

3. RESULTS

3.1. Kinematics

Kinematics of the ionized gas can be measured from strong emission lines. Since a single 47 min exposure is enough to acquire good S/N in the [O III] $\lambda 5007$ line region, we derived the velocity fields from the single datacube that showed the best spatial resolution. Figure 1 compares the broad-band images created from the datacube and the *HST* WFPC2 image along with the radio jet. The velocity field is shown in Figure 2 in three separate velocity bands from -460 to $+590 \text{ km s}^{-1}$ (relative to the quasar narrow-line emission) to separate

different clouds that are present along the same line of sight. The FWHM measurements were corrected for the $\sim 70 \text{ km s}^{-1}$ instrumental resolution. Thanks to the high spectral resolution of the data set, at least eight EELR clouds at different velocities are identified from the datacube. In the *HST* image, two of the EELR clouds are blended together since they project onto each other, and many are seen as faint knots because of the shallow exposure (300 s) and the truncation at about $+375 \text{ km s}^{-1}$ of the F656N filter.

The EELR exhibits rather complex global kinematics which cannot be explained by a simple dynamical model. The three most luminous EELR clouds in the velocity range of -230 to $+150 \text{ km s}^{-1}$ show a velocity gradient from N to S that aligns with the clouds. This gradient may be an artifact of a common disc rotation inherited from the host galaxy; but the high velocity clouds at $v > 200 \text{ km s}^{-1}$ show a velocity gradient from E to W, which is almost perpendicular to the previous one. Also, the southern cloud in the -230 to $+150 \text{ km s}^{-1}$ panels shows a velocity increase of $\sim 100 \text{ km s}^{-1}$ along NE-SW direction, which is consistent with the elongation observed in the *HST* image, thus it can be ascribed to a simple rotating disk (at another different orientation); however, the line widths also decrease along the same direction, suggesting two discrete clouds are present as hinted in the *HST* image. So overall the kinematics are disordered, but on the other hand the velocity field seems locally ordered.

There are apparently two different species of emission-line clouds—one showing relatively broad lines (FWHM $\sim 300 \text{ km s}^{-1}$), the other showing narrower lines (FWHM $\sim 100 \text{ km s}^{-1}$). The relatively broad line regions are more luminous, have smaller radial velocities ($|v| < 200 \text{ km s}^{-1}$), and are identified as spatially resolved blobs in the *HST* image. In contrast, the narrower line regions tend to have larger radial velocities ($|v| > 300 \text{ km s}^{-1}$) and are faint and seen as unresolved knots in the *HST* image. These knots feature an $H\beta$ luminosity of $\gtrsim 10^{40} \text{ erg s}^{-1}$. The most straightforward interpretation is that the narrower line regions are less massive clouds, therefore less luminous and more easily accelerated to a higher velocity; they are reminiscent of the “bullets” frequently seen in Herbig-Haro objects and local galaxies exhibiting superwinds (*e.g.*, Cecil et al. 2001) but are orders of magnitudes more energetic.

We notice that in the -230 to $+150 \text{ km s}^{-1}$ panels there is a region of very low surface-brightness emission (east of the bright emission cloud close to the center), but showing very broad lines (FWHM $> 600 \text{ km s}^{-1}$). It cannot simply be a result of blended emission lines scattered from the bright clouds nearby, since from the regions between the clouds (refer to the middle right panel of Fig. 2) we can tell that blending can increase the line width up to only $\sim 400 \text{ km s}^{-1}$. The fact that the region is along the radio jet (see Fig. 1) hints that the gas is disturbed by the radio jet.

3.2. Electron density and temperature

The luminosity-weighted average electron density can be determined from the ratio of the [O II] $\lambda\lambda 3726, 3729$ doublet, and the electron temperature can be determined from the [O III] $\lambda 4363/(\lambda 4959 + \lambda 5007)$ intensity ratio (*e.g.*, Osterbrock 1989). The S/N ratio from a single $0''.2$ pixel is not high enough to perform this kind of measurement, so we combined spectra from individual emission regions using an aperture of $0''.4$ in radius and a centered PSF as a weighting function to achieve optimal extraction. As the last step, we correct the spectra for the line-of-sight Galactic extinction (A_V

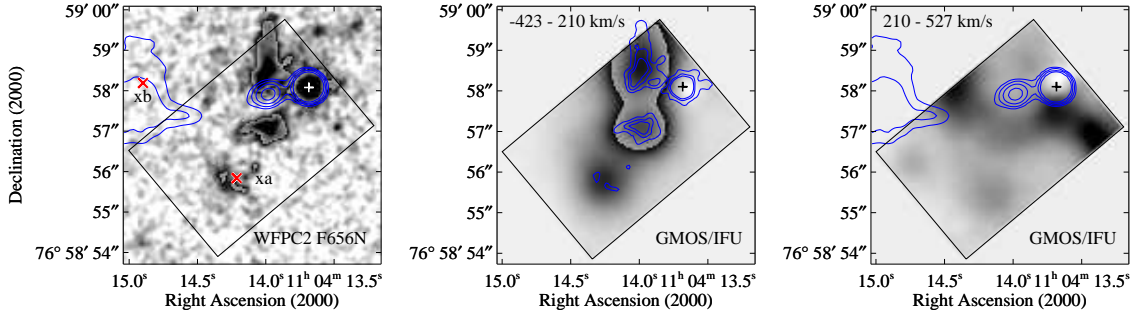


FIG. 1.— *Left*—archived *HST*/WFPC2 F656N image of 3C 249.1 (the redshifted [O III] $\lambda 5007$ falls into this filter), overlaid with contours of a VLA image at 5 GHz and $0''.35$ resolution (Gilbert et al. 2004). Contours at $0.5 \times (1, 2, 4, 8)$ mJy beam $^{-1}$. The peak of the radio continuum has been registered to the position of the quasar. The two X-ray emission regions (xa & xb) are marked in red and labeled. The gray-scale images in this and the middle panel have been allowed to wrap around to show both low-surface-brightness detail and high-surface-brightness peaks. *Middle & Right*—GMOS/IFU [O III] $\lambda 5007$ radial velocity broad-band channel maps with contours of the *HST* image and contours of the radio jet overlaid, respectively. The radial velocity range (relative to that of the nuclear narrow line region, $z = 0.3117$; negative velocities are blue shifted) is shown in each panel. The rectangles delineate the $3''.5 \times 5''$ FOV of GMOS/IFU. The crosses indicate the position of the quasar, which has been removed from the datacube (for details of the PSF removal, see § ??).

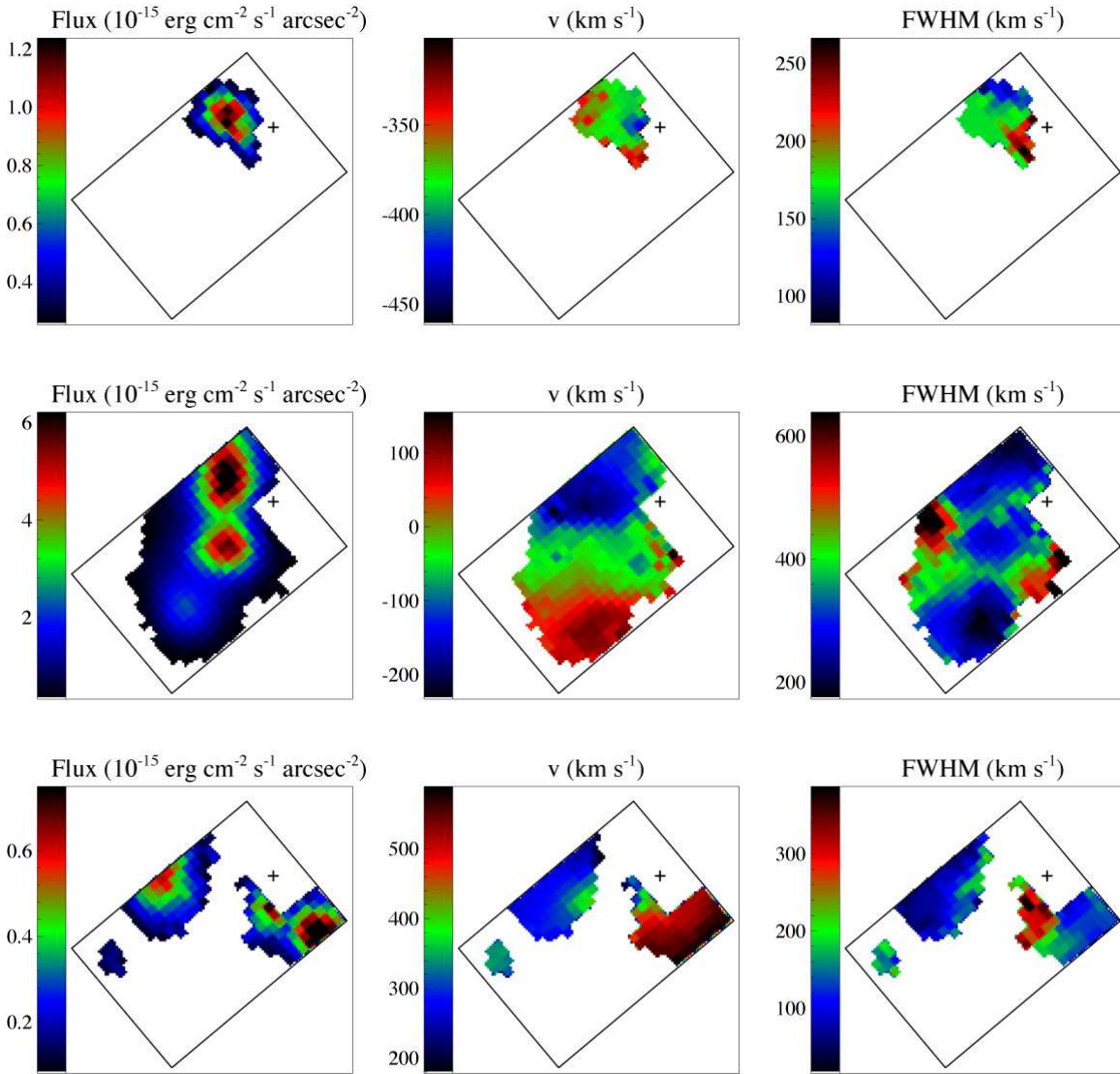


FIG. 2.— Velocity field of 3C 249.1 EELR derived from the [O III] $\lambda 5007$ region in the GMOS/IFU datacube. The three columns, from left to right, are line intensity, radial velocity (relative to that of the nuclear narrow line region) and velocity width maps. To separate different clouds that are present along the same line of sight, the velocity field is shown in three separate velocity bands (-460 to -300 km s $^{-1}$, -230 to $+150$ km s $^{-1}$ and $+180$ to $+590$ km s $^{-1}$ from the top row to the bottom row). The rectangles delineate the $3''.5 \times 5''$ FOV of GMOS/IFU. Pixels are $0''.2$ squares. The crosses indicate the position of the quasar, which has been removed from the datacube. For details see § 3.1.

= 0.112; Schlegel et al. 1998), and for the intrinsic reddening by dust associated with the clouds, which is estimated by

matching the measured $H\gamma/H\beta$ ratio with the value predicted by case-B recombination. In both cases we used the standard Galactic extinction curve of Cardelli et al. (1989). Unlike the kinematic analysis, these line ratios were extracted from the merged datacube in order to obtain better S/N for faint lines. Figure 3 shows the extraction regions, and Fig. 4 shows the extracted spectrum of EELR-*b* as an example. The spectra usually show either asymmetric line profiles or two components with different radial velocities. For both cases the line profiles usually can be fit quite well with two Gaussians. Figure 5 shows an example of our two-Gaussian model fit to the line profiles. The spectrum shows two components at different radial velocities. The relatively broader component reflects both the very broad-line cloud (§3.1) that happens to lie in the same region and the contamination from the much brighter emission clouds nearby (EELR-*a*, *b*, *c*). We measure the velocities and FWHMs of the two components from the [O III] $\lambda\lambda 4959, 5007$ lines where we have the best S/N, and freeze these parameters when fitting the much fainter [O III] $\lambda 4363$ line and the [O II] doublet. We then use the measured line fluxes to derive the electron temperatures and densities for individual clouds.

The electron temperatures of different emission regions appear fairly uniform, varying from ~ 12000 to 15000 K. We also obtained good measurements of electron densities from the relatively isolated clouds (EELR-*b*, *d* & *e*), and we found that the density varies from a few tens to a few hundreds cm^{-3} . Lower density gas has higher ionization states (as indicated by the [O III]/[O II] intensity ratios). The results are tabulated in Table 1. Clearly the pressure is quite different in different EELR clouds.

3.3. Constraints on the ionization mechanism

Recent *Chandra* ACIS observations show that 3C 249.1 has extended, highly structured X-ray emission regions, one of which follows the structure of the inner optical emission quite closely (*xa* in Fig. 1 *Left*; region *a* in Fig. 4 of Stockton et al. 2006). The X-ray emission of *xa* cannot be connected with X-ray jets frequently seen associated with radio-loud quasars, nor can it be due to electron scattering of nuclear emission. It could either be thermal bremsstrahlung emission from high-speed shocks or X-ray recombination lines from the 10^4 K photoionized gas. If it were the former case, one would expect shock-ionized gas near the X-ray emitting region.

Because of the different shapes of the ionizing-photon spectrum and different temperature regimes, ionization mechanisms (e.g., shock, “shock + precursor” and pure photoionization) can be distinguished using diagnostic diagrams involving line ratios of some optical lines. We measured line fluxes from the extracted spectra of various EELR clouds. Figure 6 compares the observations with different model grids. Unfortunately, 3C 249.1 EELR clouds (including the region associated with X-rays—EELR-*d*) all fall in the regions where the photoionization model and the “shock + precursor” model overlap, making it hard to distinguish the two, though the pure shock model can be ruled out. We will discuss the X-ray emission regions in more detail in §4.1.

We notice that the 3C 249.1 EELR shows systematically more He II emission and lower [O III] $\lambda 4363/(\lambda 4959 + \lambda 5007)$ ratios than 4C 37.43 E1, indicating a higher metallicity and a lower temperature. But aside from those lines, the spectra look remarkably similar to that of 4C 37.43 E1. The measured line fluxes are tabulated in Table 2, along with predictions from the two-phase photoionization models of Stockton et al.

(2002).

3.4. Mass of the ionized gas

The mass of the ionized clouds can be derived from their $H\beta$ luminosity and electron density. For the EELR of 3C 249.1 within the IFU field-of-view, we estimated a total $H\beta$ flux of $2.9 \times 10^{-15} \text{ erg cm}^{-2} \text{ s}^{-1}$ by assuming a constant [O III] $\lambda 5007/H\beta$ ratio of 11 (Fig. 6). The mass of the H II region is then

$$M_{\text{H}} = \frac{4\pi m_p f_{\text{H}\beta} d_L^2}{\alpha_{\text{H}\beta} n_e h\nu},$$

where m_p is the proton mass, d_L is the luminosity distance, $\alpha_{\text{H}\beta}$ is the effective recombination coefficient of $H\beta$, and $h\nu$ is the energy of a $H\beta$ photon (Osterbrock 1989). Assuming $n_e = 100 \text{ cm}^{-3}$ (§3.2) and case-B recombination at 10^4 K, we obtain $M_{\text{H}} = 6 \times 10^7 M_{\odot}$. A similar calculation for 4C 37.43 E1 yields a mass of $10^8 M_{\odot}$.

These values are probably underestimates. The mass derived above assumes a single phase cloud with an average density $\sim 100 \text{ cm}^{-3}$. However, through detailed photoionization modeling, Stockton et al. (2002) found that at least two different density regimes are required to reproduce the observed spectrum of 4C 37.43 E1: a density-bounded component with $n_e \sim 2 \text{ cm}^{-3}$ and a filling factor $f \sim 1$ and an ionization-bounded component with $n_e \sim 500 \text{ cm}^{-3}$ and $f \sim 10^{-5}$, each contributing about one half of the $H\beta$ flux. The spectra of the EELR clouds of 3C 249.1 look remarkably similar to that of 4C 37.43 E1 (see Table 2), so it is appropriate to use the same modeling results. Since the [O II] emission comes almost entirely from the high density component, the luminosity-weighted electron density $\sim 100 \text{ cm}^{-3}$ measured from [O II] $\lambda\lambda 3726, 3729$ doublet (§3.2) favors the densest material. This density could be considerably larger than the mass-weighted density (i.e., weighting $\propto n_e f$) that should be used in deriving the mass, therefore the mass derived above ($6 \times 10^7 M_{\odot}$) could have been seriously underestimated. For example, assuming $n_{e1} = 2 \text{ cm}^{-3}$ and $n_{e2} = 150 \text{ cm}^{-3}$ and both components contributing equally to the $H\beta$ luminosity, we obtain $\sim 1.5 \times 10^9 M_{\odot}$ of gas in the low density component and only $\sim 2.0 \times 10^7 M_{\odot}$ of gas in the high density component. Note that this mass is only an order of magnitude lower than the virial mass derived from assuming that the clouds are self gravitating and that the measured line widths are entirely due to motions governed by this gravitational potential (i.e., ignoring turbulence or velocity gradients along the line of sight): $M_{\text{virial}} = 5R\sigma^2/G \simeq 3.8 \times 10^{10} R_{1\text{kpc}} \text{FWHM}_{300}^2 M_{\odot}^2$. Considering the uncertainties in the simple two-phase model (e.g., the possibility of a large neutral fraction), the actual masses of individual clouds could potentially be significantly larger than the masses derived from the line fluxes, and perhaps the clouds might even be gravitationally bound. This could provide an alternative explanation for the existence of high-density gas without invoking shocks.

3.5. Kinetic energy and momentum

With the knowledge of the mass and kinematics of the emission-line clouds, we can estimate their kinetic energy and momentum. The bulk kinetic energy of a luminous EELR cloud is $E_{KE} = Mv^2/2 = 2.5 \times 10^{57} M_9 v_{500}^2 \text{ ergs}$, where M_9 is the mass of the ionized gas in units of $10^9 M_{\odot}$ and

² 1 kpc is the average radius of EELR-*c* measured from the *HST* image. The measurement was corrected for PSF broadening.

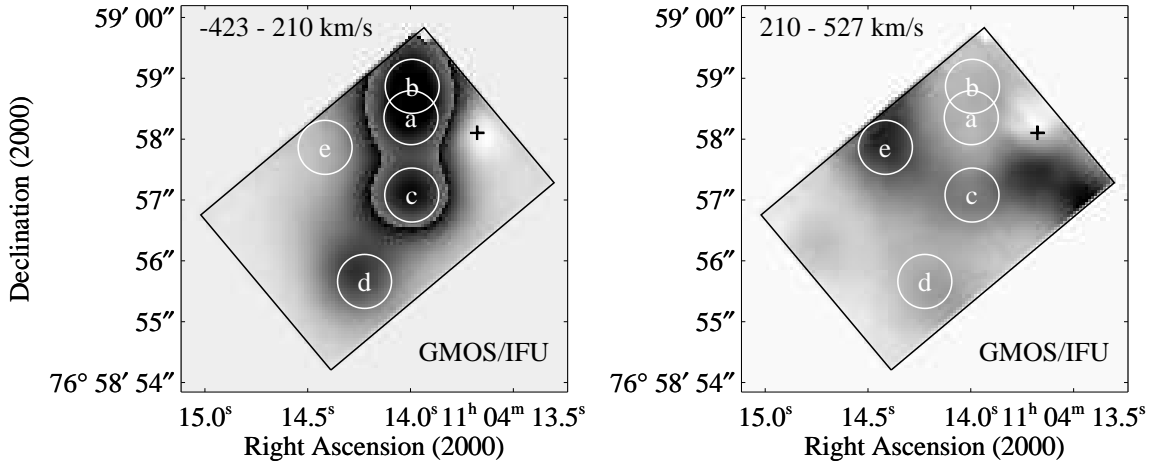


FIG. 3.— The extraction apertures of different emission-line regions. Background images are the GMOS/IFU [O III] $\lambda 5007$ radial velocity broad-band channel maps. The FOV is slightly different from the one shown in Figs. 1&2, because this one is created from the final merged datacube, while the latter is from the single exposure which had the best spatial resolution.

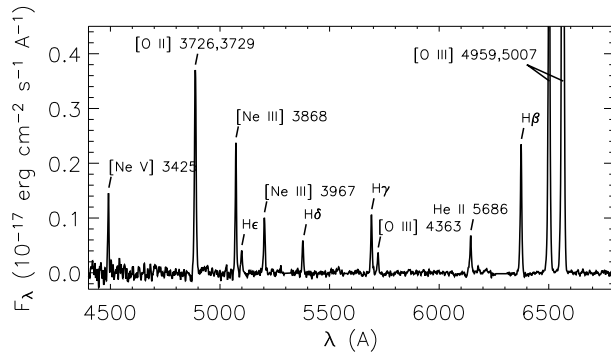


FIG. 4.— Extracted spectrum of 3C 249.1 EELR-*b* (refer to Fig. 3), with important emission lines labeled.

v_{500} is the velocity in units of 500 km s^{-1} . The kinetic energy of the unresolved kinematic substructures (“turbulent” kinetic energy) can be derived from the measured line widths, $E_{\text{turbulent}} = 6.4 \times 10^{56} M_9 \text{ FWHM}_{300}^2 \text{ ergs}$. The emission-line gas also has a thermal energy of $E_{\text{TH}} = 2.5 \times 10^{54} M_9 T_4 \text{ ergs}$ ($T_4 = T(K)/10^4 K$), which is less than 0.1% of the kinetic energy. Similarly, the total momentum is $p_{\text{kin}} = Mv = 10^{50} M_9 v_{500} \text{ dyne s}$. Whatever the driving source of this outflow is, it must have deposited this enormous amount of energy into the EELR in a short period of time ($\sim 10 \text{ Myr}$; see § 4.2). We will try to constrain the power source of this outflow in § 4.2.

4. DISCUSSION

4.1. The nature of the X-ray emission

In Fig. 7 we compare the residual *Chandra* X-ray image of 3C 249.1 and the $0''.35$ resolution radio image. This figure shows convincingly that one of the X-ray emission region, *xb*, has an intimate relationship with the radio jet. The X-ray emission is coincident with a region protruding perpendicular to the jet direction, a feature that has been noted by several authors (*e.g.*, designated X1 in Gilbert et al. 2004). Since there is a large offset ($\sim 1''.4 \approx 6.4 \text{ kpc}$) between *xb* and the nearest hotspot (N2, following Gilbert et al. 2004), it might not sim-

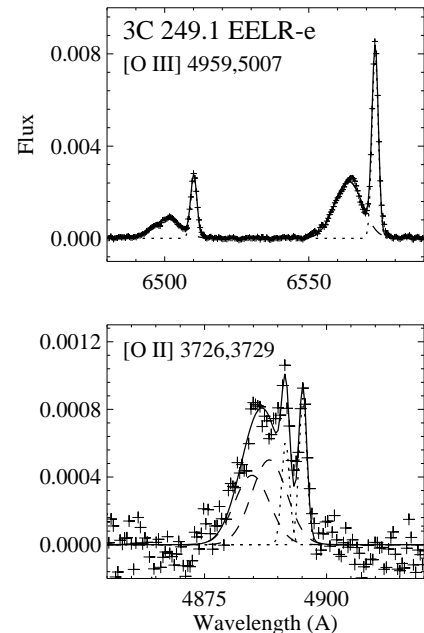


FIG. 5.— Line profiles of the [O III] $\lambda\lambda 4959, 5007$ lines (upper panel) and the [O II] $\lambda\lambda 3726, 3729$ doublet. The spectrum is extracted from 3C 249.1 EELR-*e* (see Fig. 3). Note that two velocity components are present (the relatively broader component is a result of both the very broad-line cloud discussed in §3.1 and the contamination from the much brighter emission clouds nearby). The solid curves show the best fit of four-Gaussian models, and the dashed curves and dotted curves show the “broad” and “narrow” component, respectively. The fit to the [O II] doublet has been constrained so that the relative velocity between the “broad” and “narrow” components are frozen to that determined from the fit to the [O III] lines.

ply be synchrotron radiation from the jet, but possibly a result of a gas cloud being shocked by the jet fluid.

The other X-ray emission region, *xa*, is covered by the IFU FOV. Gas kinematics, line-ratio diagnostics and its morphology all fail to provide convincing evidence of shocks, so we can not rule out the possibility that the X-ray emission is actually a result of the same recombination process as what causes

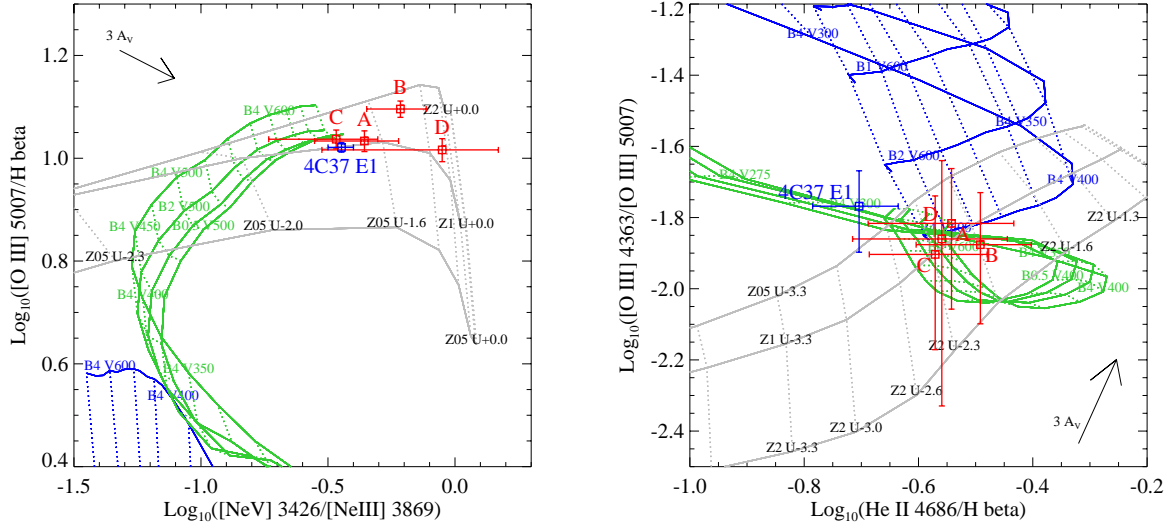


FIG. 6.— Optical line-ratio diagrams are overplotted with model grids. The dusty radiation pressure-dominated photoionization model (Groves et al. 2004), shock-only and “shock + precursor” model (Dopita & Sutherland 1996) grids are plotted in grey, blue and green, respectively. The photoionization grids assume a power-law photoionizing continuum with index $\alpha = -1.4$ and show a range of ionization parameters ($\text{Log}_{10}(U)$) for metallicities of $0.5 Z_{\odot}$, $1.0 Z_{\odot}$ and $2.0 Z_{\odot}$. The shock + precursor models assume equal contribution to the $H\beta$ line from the shocked gas and the precursor. A range of shock velocities (V_S [km s^{-1}]) and magnetic parameters ($B/n^{1/2}$ [$\mu\text{G cm}^{-3/2}$]) are covered. Line ratio measurements from four major EELR clouds of 3C 249.1 are shown in red, and the blue point shows the measurement from the Keck II/IRIS long-slit spectrum of 4C 37.43 E1 (Stockton et al. 2002). Arrows are reddening vectors of $3 A_V$, assuming the standard Galactic reddening law and $R_V = 3.1$.

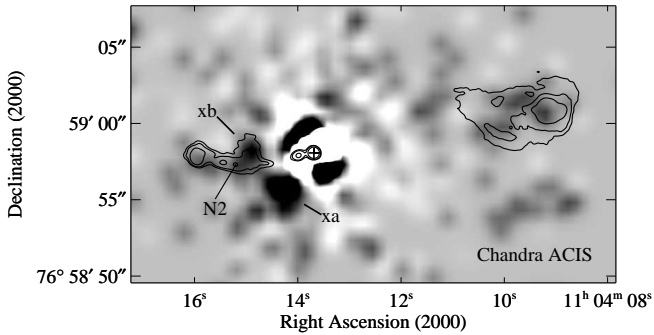


FIG. 7.— PSF-subtracted *Chandra* ACIS image of 3C 249.1 overlaid with contours of a VLA image at 5 GHz and $0''.35$ resolution (Gilbert et al. 2004). Contours at $0.5 \times (1, 2, 8)$ mJy beam $^{-1}$. The two X-ray emission regions (xa & xb) and a radio hotspot (N2) are labeled. The peak of the radio continuum has been registered to that of the X-ray emission, which is indicated by a cross, before a scaled synthetic PSF was subtracted from the X-ray image (refer to Stockton et al. 2006 for more details on the PSF subtraction).

the optical emission. If the X-ray is indeed from recombination lines, then the other high surface-brightness clouds (EELR-*a, b, c*) should also be bright in X-ray; but it is impossible to detect the emission from the *Chandra* data, since at such small radial distances their X-ray emission, if any, is completely overwhelmed by the X-rays from the quasar.

4.2. Constraints on the power source of the outflow

The dynamical timescale of the EELR can be estimated from their radial velocities and distances to the nuclei, $\tau_{dyn} \approx 10^7 D_{5kpc} \bar{v}_{500}^{-1}$ yr. Assuming an average velocity of 500 km s^{-1} is appropriate here, because the initial velocity of a galactic wind is expected to be on the level of 1000 km s^{-1} and it has since been slowed to the observed a few hundreds km s^{-1} due to mass entraining and working against gravity. At the redshift of 3C 249.1, the angular scale is 4.6 kpc arcsec $^{-1}$,

so 5 kpc is about the projected distances of the two brightest EELR clouds to the nucleus. The time scale is consistent with the age of typical luminous radio lobes, $\sim 10^7 - 10^8$ yr (Blundell & Rawlings 2000). The rate of mass outflow can be estimated assuming it is constant over the dynamical age of the ionized gas, $\dot{M} \simeq M/\tau_{dyn} = 100 M_9 D_{5kpc}^{-1} \bar{v}_{500} M_{\odot} \text{ yr}^{-1}$. Similarly the injection rate of kinetic energy is $\dot{E}_{KE} \simeq E_{KE}/\tau_{dyn} = 8 \times 10^{42} M_9 v_{500}^2 D_{5kpc}^{-1} \bar{v}_{500} \text{ ergs s}^{-1}$, and the input momentum rate is $\dot{p}_{kin} \simeq p_{kin}/\tau_{dyn} = 3 \times 10^{35} M_9 v_{500} D_{5kpc}^{-1} \bar{v}_{500} \text{ dyne}$. We emphasize that the rates can only be considered as lower limits to the actual wind energetics since the majority mass of the wind flow may not be detectable in the optical (Veilleux et al. 2005) and a substantial amount of wind-entrained ISM may be shielded from the ionizing flux of the quasar.

If the outflow is driven by a starburst, a star formation rate (SFR) of $\sim 10 M_{\odot} \text{ yr}^{-1}$ is required to deposit enough kinetic energy into the clouds, or $\sim 60 M_{\odot} \text{ yr}^{-1}$ to inject enough momentum into the ionized gas (Equations 2–3 in Veilleux et al. 2005). Since a significant fraction of the originally injected kinetic energy may have been lost to radiation and counteracting the gravitational potential, the kinetic energy is not conserved. But the wind may still conserve momentum, so the SFR of $\sim 60 M_{\odot} \text{ yr}^{-1}$ is probably more realistic. The SFR scales to an infra-red (IR) luminosity of $L_{IR}(8-1000\mu\text{m}) \approx 5.8 \times 10^9 \text{ SFR} L_{\odot} = 3.5 \times 10^{11} L_{\odot}$ (Kennicutt 1998). Is this luminosity consistent with mid-IR observations? 3C 249.1 was detected in 12, 25 and 60 μm by IRAS (Sanders et al. 1989), in 70 μm by MIPS (Shi et al. 2005), and in 100 μm by ISO (Haas et al. 2003). By using a model of two blackbody components to fit the mid-IR spectral energy distribution (SED), we obtain a total IR luminosity of $L_{IR}(8-1000\mu\text{m}) \simeq 8.6 \times 10^{11} L_{\odot}$. Thus more than 40% of the total IR luminosity must be powered by star formation to explain the input momentum rate. However, the SED peaks near 12 μm , so the IR emission is dominated by warm dust ($T \sim 100 - 200$

K) presumably directly heated by the quasar (Sanders et al. 1989). From the SED fitting, less than 23% of the total luminosity could have come from a “starburst” component with a characteristic dust temperature $T \lesssim 65$ K. Apparently the IR data argues against an on-going starburst as strong as $\sim 60 M_{\odot} \text{ yr}^{-1}$, though it doesn’t formally rule out the possibility that there was an energetic starburst which had caused the outflow but ceased not too long ago ($< \tau_{dyn} \approx 10$ Myr).

Note also that the mass outflow rate is almost an order of magnitude larger than the predicted mass injection rate from supernovae (SNe) for a $\text{SFR} \sim 60 M_{\odot} \text{ yr}^{-1}$ ($\dot{M}_{inj} \simeq 16 M_{\odot} \text{ yr}^{-1}$), which implies that the wind has entrained considerable amount of gas from the ISM. This is in contrary to the low efficiency for transporting mass out of the galaxy predicted by numerical simulations of starburst-driven galactic winds (Strickland & Stevens 2000).

Now we consider the possibility that the outflow is directly driven by the quasar of 3C 249.1. Radiation from the quasar can couple to the surrounding gas via various processes such as electric scattering, photoionization, etc. The input momentum rate from radiation pressure is $\dot{p} = 1.3 \times 10^{35} (\eta/0.1) \dot{M}_{acc}$ dyne s, where η is the radiative efficiency and \dot{M}_{acc} is the mass accretion rate of the black hole in units of $M_{\odot} \text{ yr}^{-1}$. Hence a mass accretion rate of $2.5 M_{\odot} \text{ yr}^{-1}$ is sufficient to inject enough momentum to the clouds in 10^7 yr.

This accretion rate is in agreement with the one implied by its bolometric luminosity, $\dot{M}_{acc} = 8(\eta/0.1)^{-1} M_{\odot} \text{ yr}^{-1}$ ($L_{bol} = 8 \times 10^{12} L_{\odot}$; Sanders et al. 1989).

In summary, although we cannot totally exclude a starburst origin, the available evidence favors the quasar as the power source of the outflow. If this is indeed the case, the presence of a luminous EELR may tell us something about the quasar itself. Stockton & MacKenty (1987) found that roughly one-third to one-half of all powerful, steep-spectrum radio-loud quasars show luminous EELRs, but there are clearly some for which any extended emission is quite weak. These latter cases may be those for which the quasar ignition occurred sufficiently long ago ($>$ a few 10^7 years) that the expelled gas has dissipated to the point that its surface brightness falls below our detection limit.

We thank Percy Gomez and Simon Chan for executing the queue observations, Julia Riley for providing the VLA images, and Lisa Kewley and Brent Groves for helpful discussions on the photoionization models. We thank the referee for a careful reading of the manuscript and for offering suggestions that have led to a clearer presentation. This research has been partially supported by NSF grant AST03-07335.

REFERENCES

- Blundell, K. M., & Rawlings, S. 2000, *AJ*, 119, 1111
 Cardelli, J. A., Clayton, G. C., & Mathis, J. S. 1989, *ApJ*, 345, 245
 Cecil, G., Bland-Hawthorn, J., Veilleux, S., & Filippenko, A. V. 2001, *ApJ*, 555, 338
 Di Matteo, T., Springel, V., & Hernquist, L. 2005, *Nature*, 433, 604
 Dopita, M. A., & Sutherland, R. S. 1996, *ApJS*, 102, 161
 Fabian, A. C., Crawford, C. S., Johnstone, R. M., & Thomas, P. A. 1987, *MNRAS*, 228, 963
 Gilbert, G. M., Riley, J. M., Hardcastle, M. J., Croston, J. H., Pooley, G. G., & Alexander, P. 2004, *MNRAS*, 351, 845
 Groves, B. A., Dopita, M. A., & Sutherland, R. S. 2004, *ApJS*, 153, 9
 Haas, M., et al. 2003, *A&A*, 402, 87
 Kennicutt, R. C. 1998, *ApJ*, 498, 541
 Osterbrock, D. E. 1989, *Astrophysics of Gaseous Nebulae and Active Galactic Nuclei*, Mill Valley, California: University Science Books
 Peterson, J. R., Kahn, S. M., Paerels, F. B. S., Kaastra, J. S., Tamura, T., Bleeker, J. A. M., Ferrigno, C., & Jernigan, J. G. 2003, *ApJ*, 590, 207
 Sanders, D. B., Phinney, E. S., Neugebauer, G., Soifer, B. T., & Matthews, K. 1989, *ApJ*, 347, 29
 Schlegel, D. J., Finkbeiner, D. P., & Davis, M. 1998, *ApJ*, 500, 525
 Shi, Y., et al. 2005, *ApJ*, 629, 88
 Stockton, A., Fu, H., Henry, J. P., & Canalizo, G., 2006, *ApJ*, 638, 635
 Stockton, A., & MacKenty, J. W. 1987, *ApJ*, 316, 584
 Stockton, A., MacKenty, J. W., Hu, E. M., & Kim, T.-S. 2002, *ApJ*, 572, 735
 Strickland, D. K., & Stevens, I. R. 2000, *MNRAS*, 314, 511
 Veilleux, S., Cecil, G., & Bland-Hawthorn, J. 2005, *ARA&A*, 43, 769

TABLE 1
ELECTRON DENSITY AND TEMPERATURE OF THE EELR CLOUDS.

Region	V (km s ⁻¹)	FWHM (km s ⁻¹)	T_e (K)	n_e (cm ⁻³)	[O III]/[O II]
3C 249 B	-90	300	12000 ± 800	160 ± 100	5.6
3C 249 D	+140	300	12100 ± 1300	300 ± 140	4.2
3C 249 E	+300	120	15000 ± 1500	30 ± 100	7.2

TABLE 2
OBSERVED LINE-FLUX RATIOS FOR 3C 249.1 EELR CLOUDS AND 4C 37.43 E1 AND MODELED LINE-FLUX RATIOS

Line Flux Ratios ^a	[Ne V] λ 3426	[O II] $\lambda\lambda$ 3726, 9 ^b	[Ne III] λ 3869	[O III] λ 4363	He II λ 4686	[O III] λ 5007
3C 249 A	0.44 ± 0.15	2.39 ± 0.17	1.00 ± 0.12	0.16 ± 0.07	0.29 ± 0.08	10.80 ± 0.50
3C 249 B	0.60 ± 0.15	2.22 ± 0.14	0.98 ± 0.11	0.17 ± 0.07	0.32 ± 0.07	12.47 ± 0.46
3C 249 C	0.30 ± 0.13	2.52 ± 0.19	0.89 ± 0.12	0.14 ± 0.06	0.27 ± 0.06	10.89 ± 0.46
3C 249 D	0.63 ± 0.40	2.47 ± 0.24	0.71 ± 0.13	0.14 ± 0.09	0.28 ± 0.08	10.38 ± 0.54
4C 37 E1	0.34 ± 0.04	2.86 ± 0.07	0.95 ± 0.05	0.18 ± 0.05	0.20 ± 0.03	10.50 ± 0.22
Model1 ^c	0.34	1.77	0.85	0.19	0.20	10.31
Model2	0.30	2.33	0.81	0.17	0.20	9.35

^aAll line fluxes are given as ratios to the H β flux

^bTotal flux in the [O II] doublet

^cModels 1 and 2 have 25% and 33% of the H β flux coming from the 500 cm⁻³ high-density component, see Stockton et al. 2002 (§3.4.2) for details